

Interpreting the extremely diffuse stellar distribution of Nube galaxy through fuzzy dark matter

Yu-Ming Yang,^{1,2,*} Zhao-Chen Zhang,^{1,2,†} Xiao-Jun Bi,^{1,2,‡} and Peng-Fei Yin^{1,§}

¹*Key Laboratory of Particle Astrophysics, Institute of High Energy Physics,
Chinese Academy of Sciences, Beijing 100049, China*

²*University of Chinese Academy of Sciences, Beijing 100049, China*

Recent observations have revealed an unusual stellar distribution within the almost dark dwarf galaxy Nube. The galaxy exhibits a remarkably flat stellar distribution, with an effective radius of approximately 6.9 kpc, exceeding the typical size of dwarf galaxies and even surpassing that of ultra-diffuse galaxies (UDGs) with similar stellar masses. The dynamical heating effect of fuzzy dark matter (FDM) may offer an explanation for this extremely diffuse stellar distribution in Nube. In this research, we utilize simulation techniques to investigate this issue and find that a particle mass $\mathcal{O}(1) \times 10^{-23}$ eV offers a plausible explanation for this peculiar stellar distribution anomaly.

I. INTRODUCTION

In modern physics, dark matter (DM) remains one of the most mysterious phenomena that cannot be explained by the standard model, yet it comprises roughly five times the amount of baryonic matter in the universe [1, 2]. In the standard lambda cold dark matter (Λ CDM) cosmological model, DM is postulated to consist of collisionless particles at the elementary level. This model has been highly successful in elucidating the large-scale structure of the universe and phenomena such as the cosmic microwave background radiation. However, on smaller scales, the CDM paradigm encounters numerous challenges, such as the core-cusp problem [3] and the diversity problem [4], which pertain to the effects of DM on the galactic scale.

One specific puzzle brought to light by recent observations is the stellar distribution within the almost dark dwarf galaxy Nube [5], a galaxy fortuitously discovered by the IAC Strip82 Legacy Project. Further observational analyses have revealed that Nube possesses a total stellar mass of $3.9 \pm 1.0 \times 10^8 M_\odot$. However, its surface stellar density distribution deviates significantly from that of other dwarf galaxies, exhibiting a notably flatter profile. Moreover, the effective radius of Nube measures 6.9 ± 0.8 kpc, surpassing even that of ultra-diffuse galaxies (UDGs) with comparable stellar masses [6]. Observations of Nube's morphology and its surrounding environment suggest that this galaxy is not subject to strong tidal forces, and it is located at a projected distance of approximately 435 kpc from its most likely host halo, UGC 929. These distinctive characteristics pose challenges for explaining the origin of Nube within the framework of the CDM paradigm.

As an alternative to CDM, fuzzy dark matter (FDM) [7–10] demonstrates effects on large scales that are akin

to CDM, while offering potential solutions to certain challenges faced by CDM on small scales due to its large de Broglie wavelength. A FDM halo is characterized by a soliton core [11, 12], which represents the ground state solution of the Schrödinger equation, and a NFW-like envelope composed of excited states. The interference between these different states gives rise to phenomena such as soliton oscillation, soliton random walk, and fluctuations of the granules within the NFW-like envelope [13–16]. These effects collectively contribute to fluctuations in the gravitational field, leading to the dynamical heating of the stars within the halo [17–24].

In a recent study [25], we proposed the utilization of these FDM characteristics to explain the anomalous stellar distribution in Nube. Utilizing the theoretical framework established by [17], we treated the dynamical heating phenomenon as a diffusion process affecting the stellar population in Nube. Our analysis indicates that the FDM with a mass in the range of $1 - 2 \times 10^{-23}$ eV can explain the observed data.

In this study, we utilize FDM simulation methodologies to reexamine the stellar distribution in Nube. Building upon the approach introduced by Yavetz et al. [26], we construct the initial wave function of the halo, enabling us to flexibly adjust the halo profile and the FDM particle mass utilized, without the need for deriving the initial wave function from cosmological simulations. Given that the DM mass in Nube is approximately two orders of magnitude greater than the stellar mass, we can disregard the gravitational influence of the stars. We employ the pseudo-spectral method [27] to evolve the FDM wave function, and utilize a fourth-order Runge-Kutta integrator for the evolution of stars based on the FDM gravitational potential. Our simulations confirm that a FDM particle mass of $\mathcal{O}(1) \times 10^{-23}$ eV indeed offers a plausible explanation of the anomaly observed in Nube.

This paper is organized as follows. We present our simulation setup in Sec. II. Subsequently, we showcase the results for Nube in Sec. III. A summary of our study is outlined in Sec. IV.

* yangyuming@ihep.ac.cn

† zhangzhaochen@ihep.ac.cn

‡ bixj@ihep.ac.cn

§ yinpf@ihep.ac.cn

II. SIMULATION SETUP

The equation of motion governing FDM is described as a Schrödinger-Poisson (SP) system [10]

$$\begin{aligned} i\hbar\partial_t\psi &= -\frac{\hbar^2}{2m_a}\nabla^2\psi + m_a\Phi\psi, \\ \nabla^2\Phi &= 4\pi G\rho, \quad \rho = m_a|\psi|^2. \end{aligned} \quad (1)$$

The ground state solution of this equation is known as a soliton, a feature also observed in cosmological simulations [11, 12, 28]. The density profile of the soliton is well fit by

$$\rho_{\text{sol}}(r) = \frac{\rho_c}{[1 + 0.091(r/r_c)^2]^8}, \quad (2)$$

where r_c and ρ_c denote the soliton core radius and core density, respectively. It is important to note that r_c and ρ_c are not independent but are interrelated through the scaling relation [19, 29]

$$\rho_c = 1.95 \times 10^7 M_\odot \text{kpc}^{-3} \left(\frac{m_a}{10^{-22} \text{eV}} \right)^{-2} \left(\frac{r_c}{\text{kpc}} \right)^{-4}. \quad (3)$$

Within a FDM halo, the region beyond the soliton comprises a NFW-like envelope that consists of excited state solutions of the SP equation.

A. Construction of the initial wave function of the FDM halo

The distribution of FDM can be described by the square of magnitude of the wave function solution of the SP equation. In our simulation, we require an initial wave function that can replicate the soliton+NFW density profile. To achieve this, we employ a construction method proposed by Yavetz et al.[26]. The following section briefly outlines the steps involved, with more comprehensive details available in the referenced literature.

At first, we select a target density profile as

$$\rho_{\text{in}}(r) = \begin{cases} \frac{\rho_c}{[1 + 0.091(r/r_c)^2]^8}, & r < kr_c \\ \frac{\rho_s}{(r/r_s)(1 + r/r_s)^2}, & r \geq kr_c. \end{cases} \quad (4)$$

Subject to the continuity condition at kr_c , the dynamical mass of Nube within $3R_e$ [5], and the scaling relation represented by Eq. 3, the above function is governed by only two independent parameters, chosen as k and r_s . As we discussed in the previous work [25], the influence of r_s is negligible. Therefore, for this study, we set $r_s = 10$ kpc and explore various values of k . Consequently, the target FDM profile input is solely determined by the values of m_a and k . In this research, we consider three different selections of m_a and k , as outlined in Tab. I,

TABLE I. The three models we adopt in this paper.

	m_a [10^{-23} eV]	k	M_\star [$10^8 M_\odot$]	a_i [kpc]
Model-1	1	2	8.9	3.0
Model-2	3	2	3.9	1.5
Model-3	1	3	3.9	1.5

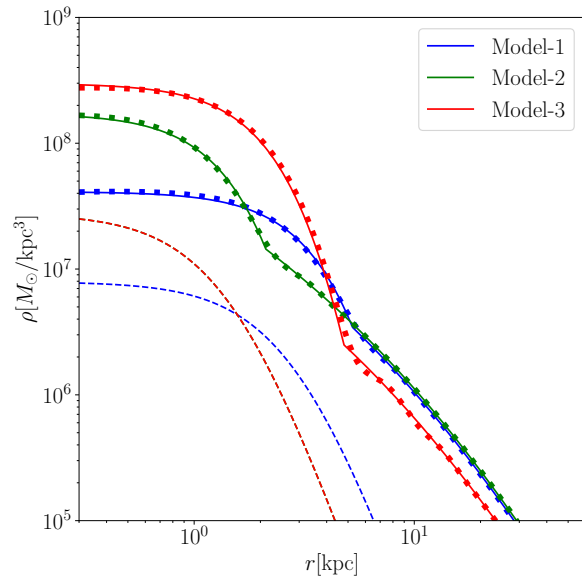


FIG. 1. The three models presented in Tab. I are distinguished by different colors. The solid lines represent the target FDM profiles used as input when creating the initial wave function. The squares on the plots indicate the output density profile obtained according to Eq. 8. Additionally, the dashed lines on the graph represent the stellar density profiles.

with the corresponding profiles depicted in Fig. 1 by the blue, green and red solid lines, respectively.

The second step involves determining the spherically symmetric gravitational potential $\Phi_{\text{in}}(r)$ that corresponds to the target density profile $\rho_{\text{in}}(r)$ and subsequently solving the time-independent Schrödinger equation under the potential $\Phi_{\text{in}}(r)$

$$-\frac{\hbar^2}{2m_a}\nabla^2\Psi_{nlm}(\mathbf{x}) + m_a\Phi_{\text{in}}(r)\Psi_{nlm}(\mathbf{x}) = E_{nl}\Psi_{nlm}(\mathbf{x}), \quad (5)$$

where the eigenmode function $\Psi_{nlm}(\mathbf{x})$ can be expressed using spherical harmonic functions

$$\Psi_{nlm}(\mathbf{x}) = R_{nl}(r)Y_l^m(\theta, \phi), \quad (6)$$

with n, l , and m the number of nodes in R_{nl} , angular, and magnetic quantum numbers, respectively. We adopt the shooting method to solve Eq. 5, which is described in Appendix. A. Then the time-dependent wave function

$\psi(t, \mathbf{x})$ can be written as a sum of these eigenmodes

$$\psi(t, \mathbf{x}) = \sum_{nlm} a_{nlm} \Psi_{nlm}(\mathbf{x}) e^{-iE_{nl}t/\hbar}. \quad (7)$$

In Eq. 7, we only consider modes with eigenenergies below a maximum energy cutoff E_c , which is set as the energy of a particle on a circular orbit at the virial radius.

The total number of eigenmodes obtained for the three models are 13469, 228607, and 7719, respectively. To simplify the subsequent analysis, we omit the m dependence of the coefficients' amplitude $|a_{nlm}|$, representing them as $|a_{nl}|$, while retaining the m dependence of their phase. This reduces the number of $|a_{nl}|$ to 533, 3489, and 373 for our three models, respectively.

The third step involves adjusting the magnitudes $|a_{nl}|$ to ensure that the random phase averaged output profile $\rho_{\text{out}}(r)$ matches the input target profile $\rho_{\text{in}}(r)$. The output profile $\rho_{\text{out}}(r)$ can be written as

$$\rho_{\text{out}}(r) = \frac{m_a}{4\pi} \sum_{nl} (2l+1) |a_{nl}|^2 R_{nl}^2(r). \quad (8)$$

We further reduce the number of free parameters $|a_{nl}|$ by dividing the energy range from the minimum value of the gravitational potential energy to the selected maximum energy cutoff into 60 bins uniformly, and assuming that the coefficients $|a_{nl}|$ of the eigenmodes within the same bin of the eigenenergy are equal. The form of Eq. 8 is a linear combination of functions $R_{nl}^2(r)$, where the coefficients of the combination are proportional to $|a_{nl}|^2$. Hence, we can utilize the non-negative least squares method to determine the optimal values of $|a_{nl}|^2$, which improves the fitting speed greatly. The maximum radius considered for fitting the input target profile is set to $1.2r_{\text{vir}}$, consistent with the selection in [26]. The resulting output profiles are illustrated in Fig. 1 using squares.

Finally, we assign a random phase dependent on m to each a_{nlm} and set $t = 0$ in Eq. 7 to obtain the initial wave function $\psi(0, \mathbf{x})$. We construct $\psi(0, \mathbf{x})$ within a simulation box of $(200 \text{ kpc})^3$ with a resolution of 512^3 . It has been verified that our simulation outcomes remain consistent even with higher resolutions or larger region box lengths.

B. Initial condition of stellar component

To incorporate the stellar component within the Nube galaxy, we adopt a Plummer profile [30] to describe the initial stellar density distribution. This profile is defined as

$$\rho_{\star}(r) = \frac{3M_{\star}}{4\pi a_i^3} \left(1 + \frac{r^2}{a_i^2}\right)^{-5/2}, \quad (9)$$

where M_{\star} and a_i represent the total stellar mass and initial effective radius of Nube, respectively. We investigate two parameter sets falling within the scatter range

of the R_e -stellar mass relation [6] for typical dwarf galaxies, as outlined in Tab. I. The corresponding profiles are depicted in Fig. 1 by the dashed lines, with Model-2 and Model-3 overlapping. It is evident from the figure that the FDM density significantly surpasses that of the stellar component across all radial distances.

We employ a total of 10^5 particles to represent the stellar component, a quantity deemed sufficient for our analysis. The acceptance-rejection method is utilized for the Monte-Carlo sampling of initial positions and velocity vectors of these particles. Position vectors are sampled according to the density profile described in Eq. 9. To obtain a stable equilibrium system as the initial condition, the velocity vectors of star particles are sampled according to the isotropic distribution function $f(\mathcal{E})$. This function is numerically computed using the the Eddington formula [31]

$$f(\mathcal{E}) = \frac{1}{\sqrt{8\pi^2}} \frac{d}{d\mathcal{E}} \int_0^{\mathcal{E}} \frac{d\Phi}{\sqrt{\mathcal{E} - \Phi}} \frac{d\rho}{d\Phi}, \quad (10)$$

where \mathcal{E} is the energy of the star particle, ρ_{\star} is the stellar density, and Φ is the total gravitational potential. Given that the observed total stellar mass of Nube is less than two percent of the dynamical mass within $3R_e$, it is evident that the gravitational potential in Nube is primarily dominated by DM. This dominance is also visually apparent from the profiles shown in Fig. 1. As a result, we simplify our analysis by considering only the contribution of the target FDM profile to the gravitational potential. We neglect the influence of the stellar component in the Eddington formula by assuming $\Phi = \Phi_{\text{in}}(r)$, which is the potential determined solely by the input FDM density profiles as illustrated Fig. 1.

After determining the initial condition of the stars, we place these 10^5 particles into the corresponding static DM potential field $\Phi_{\text{in}}(r)$ to assess the stability of the stellar distribution. We observe that the distribution remains unchanged over a period of 10 Gyr of evolution in this potential.

C. Evolution of FDM and stellar

The evolution of the FDM wave function is carried out utilizing the pseudo-spectral method as outlined in [27], with a concise summary provided in Appendix. B. We apply periodic boundary conditions within a $(200 \text{ kpc})^3$ simulation box with a resolution of 512^3 . During the evolution, feedback from stars to FDM and gravitational interactions among different stars are neglected, given that the gravitational field is predominantly dominated by DM. Consequently, only the gravitational field of FDM is taken into account. The fourth-order Runge-Kutta integrator is employed to evolve the motion of stars within this field. Any stellar particles that exceed the boundaries of the simulation box during the evolution process are removed from the simulation.

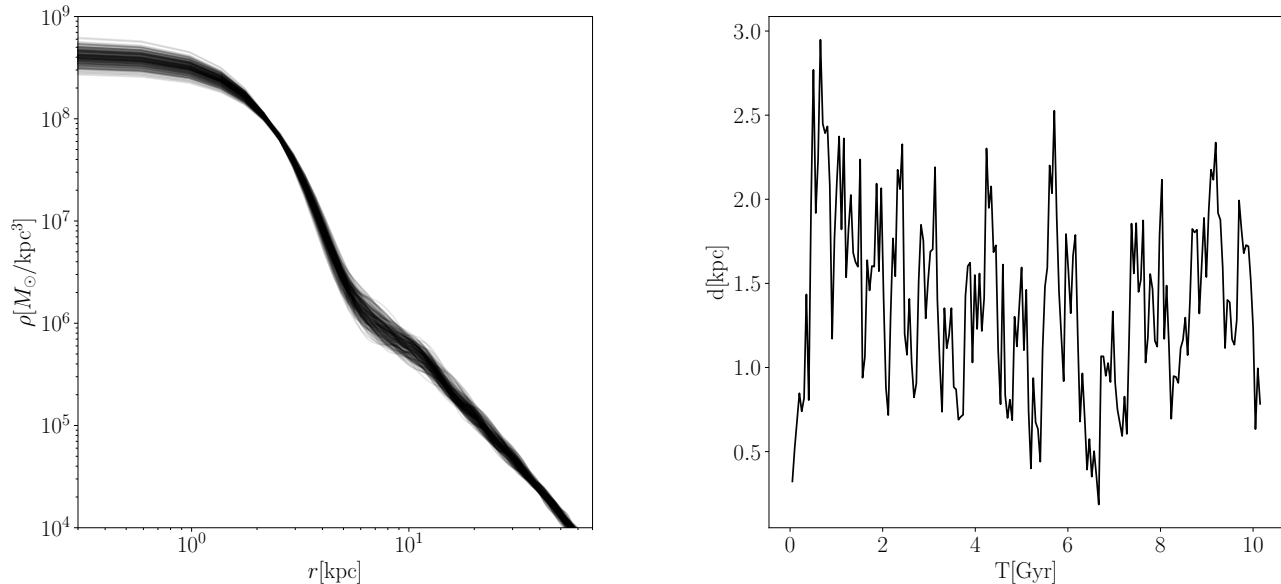


FIG. 2. Left panel: the spherically-averaged FDM density profile of 200 snapshots taken at regular intervals over the total simulation time of 10.2 Gyr. Right panel: the separation between the soliton center and the center of mass of the total halo at these 200 time points.

The time steps for the evolution of the FDM wave function and stellar particles are set to be $\Delta t_{\text{FDM}} = 0.971 \text{ Myr}$ and $\Delta t_{\star} = 0.097 \text{ Myr}$, respectively. Consequently, after one step of evolution of the FDM wave function, the stellar particles undergo evolution for ten steps. It is assumed that during these ten steps of stellar evolution, the density distribution of FDM and the corresponding gravitational field remain unchanged over time. It has been verified that the results remain robust even with smaller time steps. Each simulation is conducted for a total duration of 10.2 Gyr, corresponding to the age of Nube. Further details regarding the evolution of FDM and stellar particles can be found in Appendix. B.

III. RESULTS

In our original simulation, we note that the initial velocity of the halo constructed in Sec. II A is not zero. The presence of a non-zero velocity is explained by the interference between states with odd and even parity. Actually, in order to realize a halo with zero velocity by the form of Eq. 7, the initial phase of each term should be adjusted carefully. However, as we have assigned the phase randomly this leads to a non-zero initial velocity of the halo. This issue will be addressed in another work. To compensate for this non-zero velocity, we introduce a Galilean boost by multiplying a factor of $e^{im_a \mathbf{v} \cdot \mathbf{x} / \hbar}$ to $\psi(0, \mathbf{x})$ and adjusting \mathbf{v} to minimize the overall movement of the halo. However, since the gravitational potential is dominated by DM, the center of mass of the stellar par-

ticles moves in accordance with the gravitational potential well. We find that whether or not this adjustment is made does not significantly affect the final distribution of stars in the simulation. Therefore, we implement this adjustment only in Model-3 and omit it in Model-1 and Model-2. As an illustration, we focus on Model-3 to showcase the properties of our simulation outcomes.

In the left panel of Fig. 2, the spherically-averaged FDM density profiles of 200 snapshots taken at regular intervals over the total simulation time of 10.2 Gyr is depicted. The right panel of Fig. 2 displays the separation between the soliton center and the center of mass of the total halo at these 200 time points. This visualization allows for an intuitive observation of the soliton oscillation and random walk effects.

The top row of Fig. 3 displays the FDM density field $\rho = m_a |\psi|^2$ in $z = 0$ plane at six different snapshots. This visualization captures the dynamic behavior of the soliton and granules within the system. The soliton appears as a distinct, dense region in the center, while the granules exhibit a more diffuse and fluctuating distribution around it. As time progresses, the soliton undergoes oscillations and random movements, while the granules also continue to evolve. These fluctuations in the density field result in corresponding fluctuations in the gravitational field, which in turn affect the distribution of stellar particles in the system [17]. The bottom row of Fig. 3 illustrates how the projected positions of the stellar particles onto the x-y plane evolve over time, showing an expansion of the stellar distribution driven by the dy-

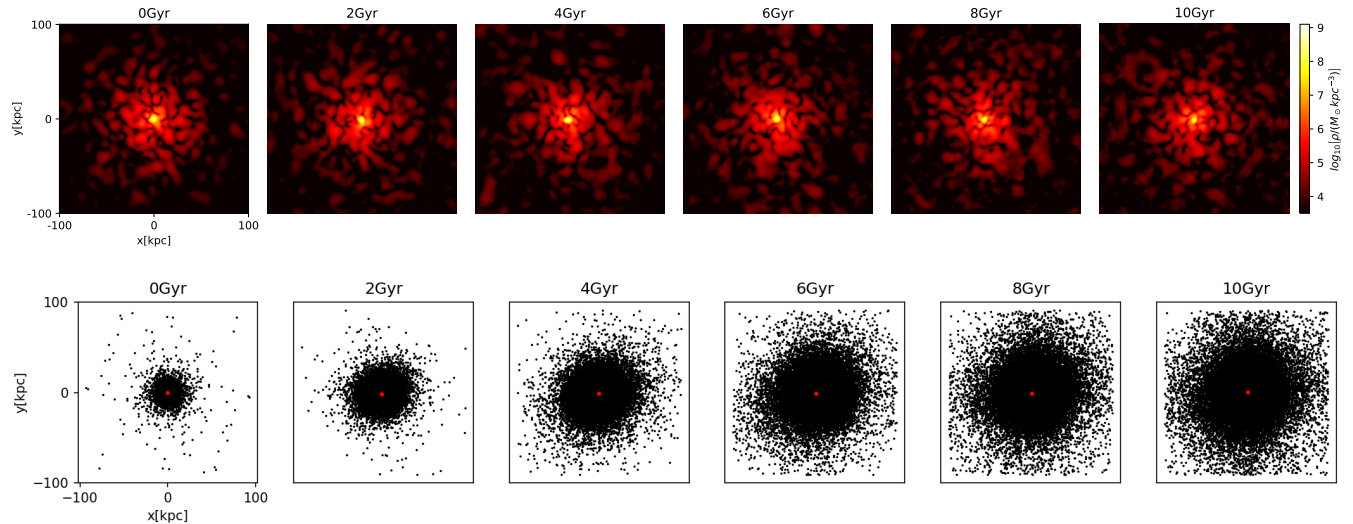


FIG. 3. Top row: the FDM density field $\rho = m_a |\psi|^2$ in the $z = 0$ plane at six different snapshots throughout the entire simulation duration. Bottom row: the projected positions of the stellar particles onto the x - y plane are depicted in various panels, with each panel displaying the distribution of stellar particles at different snapshots. The red dot indicates the position of the center of mass of the stellar distribution.

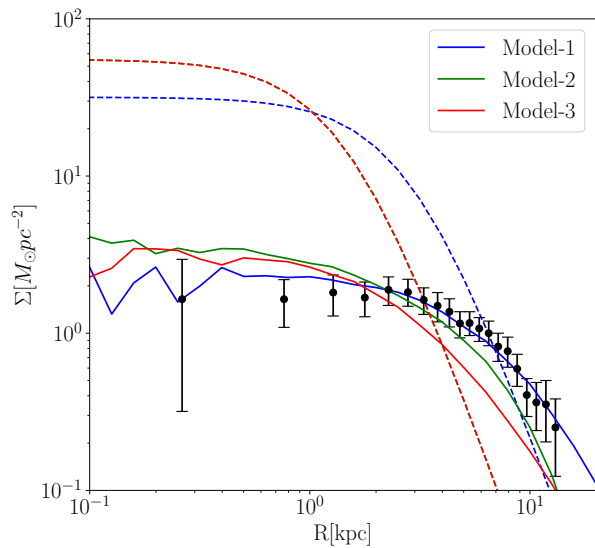


FIG. 4. The initial (dashed lines) and final (solid lines) 2D stellar density profiles of our three models are depicted. The color scheme aligns with the colors used in Fig. 1. The error bars in the graph represent the observational results.

namical heating effect.

In order to compare the simulation results with observational data, we present the initial and final 2D stellar density profiles of our three models in Fig. 4, where the initial profile of Model-2 and Model-3 overlap. Our analysis reveals that Model-1 aligns best with the observed data, while Model-2 and Model-3 exhibit higher or lower

densities than observed in the inner and outer regions, respectively. In the outer region, the lower densities observed in Model-2 and Model-3 compared to the observational data is due to an excess of stars being pushed into the region $R > 10$ kpc, as can be clearly seen in the bottom row of Fig. 3. Consequently, a natural consequence of Model-1 is the presence of numerous stars in the region $R > 10$ kpc. However, the surface density in this area is too low to be detected by current observations. Future observations may potentially identify this dark region and assess the validity of the FDM explanation.

IV. SUMMARY

Recent observations have unveiled an anomalous stellar distribution in the nearly dark dwarf galaxy Nube, posing a challenge to the CDM model. In this study, we employ the dynamical heating effect of FDM to elucidate this anomaly through FDM simulation. The method employed here offers a flexible framework for adjusting the mass of FDM particles, enabling the construction of halos with arbitrary profiles and total masses. Our findings suggest that an FDM particle mass on the order of $\mathcal{O}(1) \times 10^{-23}$ eV offers a plausible explanation for the anomaly. A natural consequence of our explanation is that the presence of numerous stars in the region $R > 10$ kpc. Future observations have the potential to uncover this obscured region and evaluate the validity of the FDM hypothesis.

There are other studies which also prefer a FDM with mass at the order of $\mathcal{O}(1) \times 10^{-23}$ eV [32–36], which are consistent with our present work as well as our previous

work [25]. However, there are also numerous stringent constraints from investigations involving the Lyman- α forest [37], subhalo mass function [38], and dynamical heating effect in dwarf galaxies [21], which require the FDM mass significantly higher than our results. Nevertheless, some of these studies are currently under intense debate. Further information on these debates can be found in the Refs. [25, 35, 36]. The inconsistency

among the studies may be attributed to the uncertainties in observations as well as imperfections in the theory itself. Further research is needed to address these issues.

ACKNOWLEDGMENTS

This work is supported by the National Natural Science Foundation of China under grant No. 12175248.

-
- [1] F. Zwicky, Die Rotverschiebung von extragalaktischen Nebeln, *Helvetica Physica Acta* **6**, 110 (1933).
- [2] V. C. Rubin and J. Ford, W. Kent, Rotation of the Andromeda Nebula from a Spectroscopic Survey of Emission Regions, *Astrophys. J.* **159**, 379 (1970).
- [3] W. J. G. de Blok, The Core-Cusp Problem, *Advances in Astronomy* **2010**, 1–14 (2010).
- [4] K. A. Oman, J. F. Navarro, A. Fattahi, C. S. Frenk, T. Sawala, S. D. M. White, R. Bower, R. A. Crain, M. Furlong, M. Schaller, J. Schaye, and T. Theuns, The unexpected diversity of dwarf galaxy rotation curves, *Monthly Notices of the Royal Astronomical Society* **452**, 3650–3665 (2015).
- [5] M. Montes *et al.*, An almost dark galaxy with the mass of the Small Magellanic Cloud, *Astronomy & Astrophysics* **681**, A15 (2024).
- [6] N. Chamba, I. Trujillo, and J. H. Knapen, Are ultra-diffuse galaxies milky way-sized?, *Astronomy & Astrophysics* **633**, L3 (2020).
- [7] W. Hu, R. Barkana, and A. Gruzinov, Fuzzy Cold Dark Matter: The Wave Properties of Ultralight Particles, *Physical Review Letters* **85**, 1158–1161 (2000).
- [8] P. J. E. Peebles, Fluid Dark Matter, *Astrophys. J.* **534**, L127 (2000), [arXiv:astro-ph/0002495](https://arxiv.org/abs/astro-ph/0002495) [astro-ph].
- [9] L. Hui, J. P. Ostriker, S. Tremaine, and E. Witten, Ultralight scalars as cosmological dark matter, *Physical Review D* **95**, 10.1103/physrevd.95.043541 (2017).
- [10] L. Hui, Wave Dark Matter, *Annual Review of Astronomy and Astrophysics* **59**, 247–289 (2021).
- [11] H.-Y. Schive, T. Chiueh, and T. Broadhurst, Cosmic structure as the quantum interference of a coherent dark wave, *Nature Physics* **10**, 496–499 (2014).
- [12] H.-Y. Schive, M.-H. Liao, T.-P. Woo, S.-K. Wong, T. Chiueh, T. Broadhurst, and W.-Y. P. Hwang, Understanding the Core-Halo Relation of Quantum Wave Dark Matter from 3D Simulations, *Physical Review Letters* **113**, 10.1103/physrevlett.113.261302 (2014).
- [13] X. Li, L. Hui, and T. D. Yavetz, Oscillations and random walk of the soliton core in a fuzzy dark matter halo, *Physical Review D* **103**, 10.1103/physrevd.103.023508 (2021).
- [14] I.-K. Liu, N. P. Proukakis, and G. Rigopoulos, Coherent and incoherent structures in fuzzy dark matter haloes, *Monthly Notices of the Royal Astronomical Society* **521**, 3625–3647 (2023).
- [15] J. Veltmaat, J. C. Niemeyer, and B. Schwabe, Formation and structure of ultralight bosonic dark matter halos, *Physical Review D* **98**, 10.1103/physrevd.98.043509 (2018).
- [16] H.-Y. Schive, T. Chiueh, and T. Broadhurst, Soliton Random Walk and the Cluster-Stripping Problem in Ultralight Dark Matter, *Physical Review Letters* **124**, 10.1103/physrevlett.124.201301 (2020).
- [17] B. Bar-Or, J.-B. Fouvry, and S. Tremaine, Relaxation in a Fuzzy Dark Matter Halo, *The Astrophysical Journal* **871**, 28 (2019).
- [18] A. A. El-Zant, J. Freundlich, F. Combes, and A. Halle, The effect of fluctuating fuzzy axion haloes on stellar dynamics: a stochastic model, *Monthly Notices of the Royal Astronomical Society* **492**, 877–894 (2019).
- [19] D. Dutta Chowdhury, F. C. van den Bosch, P. van Dokkum, V. H. Robles, H.-Y. Schive, and T. Chiueh, On the Dynamical Heating of Dwarf Galaxies in a Fuzzy Dark Matter Halo, *The Astrophysical Journal* **949**, 68 (2023).
- [20] D. Dutta Chowdhury, F. C. van den Bosch, V. H. Robles, P. van Dokkum, H.-Y. Schive, T. Chiueh, and T. Broadhurst, On the Random Motion of Nuclear Objects in a Fuzzy Dark Matter Halo, *The Astrophysical Journal* **916**, 27 (2021).
- [21] D. J. E. Marsh and J. C. Niemeyer, Strong Constraints on Fuzzy Dark Matter from Ultrafaint Dwarf Galaxy Eridanus II, *Physical Review Letters* **123**, 10.1103/physrevlett.123.051103 (2019).
- [22] B. V. Church, P. Mocz, and J. P. Ostriker, Heating of milky way disc stars by dark matter fluctuations in cold dark matter and fuzzy dark matter paradigms, *Monthly Notices of the Royal Astronomical Society* **485**, 2861–2876 (2019).
- [23] N. Dalal and A. Kravtsov, Excluding fuzzy dark matter with sizes and stellar kinematics of ultrafaint dwarf galaxies, *Phys. Rev. D* **106**, 063517 (2022).
- [24] B. T. Chiang, H.-Y. Schive, and T. Chiueh, Soliton oscillations and revised constraints from Eridanus II of fuzzy dark matter, *Physical Review D* **103**, 10.1103/physrevd.103.103019 (2021).
- [25] Y. M. Yang, X. J. Bi, and P. F. Yin, A theoretical perspective on the almost dark galaxy Nube: exploring the fuzzy dark matter model, *JCAP* **07**, 054, [arXiv:2404.05375](https://arxiv.org/abs/2404.05375) [astro-ph.CO].
- [26] T. D. Yavetz, X. Li, and L. Hui, Construction of wave dark matter halos: Numerical algorithm and analytical constraints, *Physical Review D* **105**, 10.1103/physrevd.105.023512 (2022).
- [27] F. Edwards, E. Kendall, S. Hotchkiss, and R. Easther, Pylultralight: a pseudo-spectral solver for ultralight dark matter dynamics, *Journal of Cosmology and Astroparticle Physics* **2018** (10), 027–027.
- [28] P. Mocz, M. Vogelsberger, V. H. Robles, J. Zavala, M. Boylan-Kolchin, A. Fialkov, and L. Hernquist, Galaxy formation with BECDM – I. Turbulence and relaxation

of idealized haloes, *Monthly Notices of the Royal Astronomical Society* **471**, 4559–4570 (2017).

- [29] F. S. Guzman and L. A. Urena-Lopez, Gravitational Cooling of Self-gravitating Bose Condensates, *The Astrophysical Journal* **645**, 814–819 (2006).
- [30] H. C. Plummer, On the problem of distribution in globular star clusters, *Monthly Notices of the Royal Astronomical Society* **71**, 460 (1911).
- [31] A. S. Eddington, The distribution of stars in globular clusters, *Monthly Notices of the Royal Astronomical Society* **76**, 572 (1916).
- [32] V. Lora, J. Magaña, A. Bernal, F. Sánchez-Salcedo, and E. Grebel, On the mass of ultra-light bosonic dark matter from galactic dynamics, *Journal of Cosmology and Astroparticle Physics* **2012** (02), 011–011.
- [33] A. X. González-Morales, D. J. E. Marsh, J. Peñarrubia, and L. A. Ureña-López, Unbiased constraints on ultralight axion mass from dwarf spheroidal galaxies, *Monthly Notices of the Royal Astronomical Society* **472**, 1346–1360 (2017).
- [34] R. Hložek, D. J. E. Marsh, and D. Grin, Using the full power of the cosmic microwave background to probe axion dark matter, *Monthly Notices of the Royal Astronomical Society* **476**, 3063–3085 (2018).
- [35] B. T. Chiang, J. P. Ostriker, and H.-Y. Schive, Can ultralight dark matter explain the age–velocity dispersion relation of the Milky Way disc: A revised and improved treatment, *Monthly Notices of the Royal Astronomical Society* **518**, 4045–4063 (2022).
- [36] A. Bañares-Hernández, A. Castillo, J. Martin Camalich, and G. Iorio, Confronting fuzzy dark matter with the rotation curves of nearby dwarf irregular galaxies, *Astronomy & Astrophysics* **676**, A63 (2023).
- [37] K. K. Rogers and H. V. Peiris, Strong Bound on Canonical Ultralight Axion Dark Matter from the Lyman-Alpha Forest, *Physical Review Letters* **126**, 10.1103/physrevlett.126.071302 (2021).
- [38] E. O. Nadler, V. Gluscevic, K. K. Boddy, and R. H. Wechsler, Constraints on Dark Matter Microphysics from the Milky Way Satellite Population, *The Astrophysical Journal Letters* **878**, L32 (2019).

Appendix A: Solution of the time-independent Schrödinger equation

In order to derive the initial wave functions of FDM, we utilize the shooting method to solve the time-independent Schrödinger equation represented by Eq. 5. Substituting Eq. 6 into Eq. 5, we derive the equation governing the initial radial wave function $R_{nl}(r)$ as

$$-\frac{\hbar^2}{2m_a} \frac{1}{r^2} \frac{d}{dr} \left(r^2 \frac{dR_{nl}}{dr} \right) + \left[\frac{\hbar^2}{2m_a} \frac{l(l+1)}{r^2} + m_a \Phi_{\text{in}} \right] R_{nl} = E_{nl} R_{nl}, \quad (\text{A1})$$

where Φ_{in} is the initial gravitational potential determined by Eq. 4. The boundary conditions of this equation are specified as

$$|R_{nl}(0)| < +\infty, \quad \lim_{r \rightarrow \infty} r R_{nl}(r) = 0. \quad (\text{A2})$$

The radial wave function R_{nl} is normalized according to the condition

$$\int_0^\infty r^2 R_{nl}^2(r) dr = 1. \quad (\text{A3})$$

Subsequently, we define an auxiliary function $u_{nl} \equiv r R_{nl}$ and rewrite Eq. A1 as

$$-\frac{\hbar^2}{2m_a} \frac{d^2 u_{nl}}{dr^2} + \left[\frac{\hbar^2}{2m_a} \frac{l(l+1)}{r^2} + m_a \Phi_{\text{in}} \right] u_{nl} = E_{nl} u_{nl}. \quad (\text{A4})$$

To simplify the solution procedure, we non-dimensionalize Eq. A4 using the same length, time, and mass scales as those used in the FDM wave function evolution in Appendix. B, which is also consistent with those in [27]. These scales are

$$\mathcal{L} \equiv \left(\frac{8\pi\hbar^2}{3m_a^2 H_0^2 \Omega_{m0}} \right)^{1/4} \simeq 121 \left(\frac{10^{-23} \text{eV}}{m_a} \right)^{1/2} \text{ kpc}, \quad (\text{A5})$$

$$\mathcal{T} \equiv \left(\frac{8\pi}{3H_0^2 \Omega_{m0}} \right)^{1/2} \simeq 75.5 \text{ Gyr}, \quad (\text{A6})$$

$$\mathcal{M} \equiv \frac{1}{G} \left(\frac{8\pi}{3H_0^2 \Omega_{m0}} \right)^{-1/4} \left(\frac{\hbar}{m_a} \right)^{3/2} \simeq 7 \times 10^7 \left(\frac{10^{-23} \text{eV}}{m_a} \right)^{3/2} M_\odot. \quad (\text{A7})$$

The dimensionless form of Eq. A4 is expressed as

$$-\frac{1}{2} \frac{d^2 \tilde{u}_{nl}}{d\tilde{r}^2} + \left[\frac{l(l+1)}{2\tilde{r}^2} + \tilde{\Phi}_{\text{in}} \right] \tilde{u}_{nl} = \tilde{E}_{nl} \tilde{u}_{nl}, \quad (\text{A8})$$

where

$$\tilde{u}_{nl} \equiv \frac{\mathcal{T} \sqrt{m_a G}}{\mathcal{L}} u_{nl}, \quad \tilde{r} \equiv \frac{r}{\mathcal{L}}, \quad \tilde{\Phi}_{\text{in}} = \frac{m_a \mathcal{T}}{\hbar} \Phi_{\text{in}}, \quad \tilde{E}_{nl} \equiv \frac{\mathcal{T}}{\hbar} E_{nl}. \quad (\text{A9})$$

Introducing another auxiliary function \tilde{v}_{nl} enables us to reformulate Eq. A8 as a system of two first-order differential equations

$$\begin{cases} \frac{d\tilde{u}_{nl}}{d\tilde{r}} = \tilde{v}_{nl}, \\ \frac{d\tilde{v}_{nl}}{d\tilde{r}} = 2 \left[\frac{l(l+1)}{2\tilde{r}^2} + \tilde{\Phi}_{\text{in}} - \tilde{E}_{nl} \right] \tilde{u}_{nl}. \end{cases} \quad (\text{A10})$$

The normalization condition and boundary conditions of R_{nl} equivalently expressed in terms of those of \tilde{u}_{nl} as

$$\int_0^\infty \tilde{u}_{nl}^2 d\tilde{r} = \frac{\mathcal{L}^3}{m_a G \mathcal{T}^2}, \quad \tilde{u}_{nl}(0) = 0, \quad \lim_{\tilde{r} \rightarrow \infty} \tilde{u}_{nl}(\tilde{r}) = 0. \quad (\text{A11})$$

Eqs. A10 and A11 can be viewed as an eigenvalue problem. For a given value of \tilde{E}_{nl} , the boundary condition at $\tilde{r} = \infty$ and the normalization condition together uniquely

determine a solution to Eq. A10. However, the boundary condition at $\tilde{r} = 0$ is only satisfied for certain specific values of \tilde{E}_{nl} , which correspond to the eigenvalues of Eq. A10.

In practical operations, when considering a specific value of l and \tilde{E}_{nl} , we numerically solve Eq. A10 within a finite grid spanning from $\tilde{r}_1 = r_1/\mathcal{L}$ to $\tilde{r}_2 = r_2/\mathcal{L}$, where r_1 and r_2 are selected as 0.01 kpc and $4r_{\text{vir}}$, respectively. We have verified that the solutions remain almost unchanged even when employing a broader region for numerical computations. At the outer boundary \tilde{r}_2 , we impose the boundary conditions as $\tilde{u}_{nl}(\tilde{r}_2) = 0$ and $\tilde{v}_{nl}(\tilde{r}_2) = \tilde{v}_0$, where the value of \tilde{v}_0 is arbitrarily chosen. This value will be appropriately rescaled later by applying the normalization condition. Subsequently, we evolve the functions \tilde{u}_{nl} and \tilde{v}_{nl} according to Eq. A10 using the fourth-order Runge-Kutta integrator to determine the value of $\tilde{u}_{nl}(\tilde{r}_1)$. To determine the correct \tilde{E}_{nl} as an eigenvalue, we utilize the bisection method to iteratively adjust \tilde{E}_{nl} such that $\tilde{u}_{nl}(\tilde{r}_1)$ approaches zero. This iterative procedure enables the determination of the eigenvalue \tilde{E}_{nl} that satisfies the inner boundary condition $\tilde{u}_{nl}(\tilde{r}_1) = 0$.

In order to ensure a comprehensive exploration of possible energy levels, we exploit the feature that the energy spacing between levels increases as the energy decreases. Thus, we systematically search for eigenenergies starting from the highest value and progressing towards the lowest value. For a given l value, we commence the procedure from an initial assumed maximum

energy cutoff \tilde{E}_c , which represents the energy of a particle in a circular orbit at the virial radius. Initially, we search for the highest energy eigenvalue \tilde{E}_N in intervals $[\tilde{E}_c - (j-1)\Delta_c, \tilde{E}_c - j\Delta_c]$, where j is a positive integer that incrementally increases from 1 and Δ_c is a sufficiently small value, until \tilde{E}_N is identified. Subsequently, we continue the search for the second-highest eigenvalue \tilde{E}_{N-1} in intervals $[\tilde{E}_N - (j-1)\Delta_N, \tilde{E}_N - j\Delta_N]$, where Δ_N is set as $\tilde{E}_c - \tilde{E}_N$, until \tilde{E}_{N-1} is identified. Then we set $\Delta_{N-1} = \tilde{E}_N - \tilde{E}_{N-1}$ and search for \tilde{E}_{N-2} in intervals $[\tilde{E}_{N-1} - (j-1)\Delta_{N-1}, \tilde{E}_{N-1} - j\Delta_{N-1}]$. This iterative procedure is repeated until the eigenmode with the lowest eigenenergy \tilde{E}_0 is discovered.

Appendix B: FDM and stellar evolution

We utilize the pseudo-spectral method, as detailed in [27], to evolve the FDM wave function. Here is a brief overview of the methodology. By using the length, time, and mass scales defined in Eq. A5, Eq. A6, and Eq. A7, respectively, we can non-dimensionize the time-dependent Schrödinger equation as follows

$$i \frac{\partial}{\partial \tilde{t}} \tilde{\psi}(\tilde{t}, \tilde{\mathbf{x}}) = -\frac{1}{2} \tilde{\nabla}^2 \tilde{\psi}(\tilde{t}, \tilde{\mathbf{x}}) + \tilde{\Phi}(\tilde{t}, \tilde{\mathbf{x}}) \tilde{\psi}(\tilde{t}, \tilde{\mathbf{x}}), \quad (\text{B1})$$

where

$$\tilde{\psi} \equiv \mathcal{T} \sqrt{m_a G} \psi, \quad \tilde{\Phi} \equiv \frac{m_a \mathcal{T}}{\hbar} \Phi, \quad \tilde{t} = \frac{t}{\mathcal{T}}, \quad \tilde{\mathbf{x}} \equiv \frac{\mathbf{x}}{\mathcal{L}}. \quad (\text{B2})$$

The wave function can be evolved as

$$\tilde{\psi}(\tilde{t} + \Delta\tilde{t}_{\text{FDM}}, \tilde{\mathbf{x}}) = \exp\left[-\frac{i\Delta\tilde{t}_{\text{FDM}}}{2} \tilde{\Phi}(\tilde{t} + \Delta\tilde{t}_{\text{FDM}}, \tilde{\mathbf{x}})\right] \mathcal{F}^{-1} \left\{ \exp\left(-\frac{i\Delta\tilde{t}_{\text{FDM}}}{2} k^2\right) \mathcal{F} \left[\exp\left[-\frac{i\Delta\tilde{t}_{\text{FDM}}}{2} \tilde{\Phi}(\tilde{t}, \tilde{\mathbf{x}})\right] \tilde{\psi}(\tilde{t}, \tilde{\mathbf{x}}) \right] \right\}, \quad (\text{B3})$$

where \mathcal{F} and \mathcal{F}^{-1} represent the Fourier and inverse Fourier transformations, respectively. The gravitational field generated by FDM at dimensionless time \tilde{t} can be calculated as

$$\tilde{\Phi}(\tilde{t}, \tilde{\mathbf{x}}) = \mathcal{F}^{-1} \left\{ -\frac{1}{k^2} \mathcal{F} \left[4\pi \left| \tilde{\psi}(\tilde{t}, \tilde{\mathbf{x}}) \right|^2 \right] \right\}. \quad (\text{B4})$$

Using this approach, we calculate the wave function and gravitational field at grid points at time t . To determine the acceleration experienced by a star particle

at any position within the simulated box, we interpolate the gravitational field at grid points to obtain a continuous field throughout the box. The acceleration of a star at position $\mathbf{x}(t)$ can be calculated using Newton's second law $\mathbf{a}(t) = -\nabla\Phi(t, \mathbf{x}(t))$. Subsequently, the position and velocity of this star particle at $t + \Delta t_*$ can be determined based on $\mathbf{x}(t)$, $\mathbf{v}(t)$ and $\mathbf{a}(t)$. To enhance the accuracy of particle evolution, we employ the fourth-order Runge-Kutta method in the calculation.